Mathematics

AIMS Mathematics, 11(6): 15302–15323.
DOI: 10.3934/math.2026629
Received: 15 March 2026
Revised: 19 May 2026
Accepted: 27 May 2026
Published: 01 June 2026

http://www.aimspress.com/journal/Math

Research article

Nonlinear stability and critical penetration analysis of mixed autonomous traffic with anticipative optimal-velocity control

Shihlin Lin*

Graduate Institute of Vehicle Engineering, National Changhua University of Education, No. 1, Jin-De Road, Changhua City, Taiwan

* **Correspondence:** Email: lin040@cc.ncue.edu.tw.

Abstract: In this study, we developed a nonlinear mean-field penetration model for car-following dynamics to examine how partial penetration of connected and autonomous vehicles (CAVs) alters traffic-wave stability on a single-lane ring road. The model extends classical optimal-velocity dynamics through two penetration-scaled mechanisms: An anticipative headway correction and a cooperative speed-difference damping term. The homogeneous equilibrium was derived in closed form, and linearization with Fourier perturbations yielded an explicit characteristic equation. A long-wave expansion then yielded a tractable stability theorem together with a closed-form formula for the critical penetration threshold. For the baseline parameters $a = 2.8$, $\sigma = 0.8$, $\kappa = 2.0$, $h = 13\ \mathrm{m}$, $v_{\max} = 30\ \mathrm{m/s}$, $s_c = 10\ \mathrm{m}$, and $\ell = 5\ \mathrm{m}$, the asymptotic threshold was $p_c \approx 0.173$, which was close to the exact discrete threshold $p_c \approx 0.171$ obtained from the linearized finite-ring system. Ring-road simulations confirmed the theoretical trend: When $p = 0$, stop-and-go waves persist and reduce the mean speed to $19.17\ \mathrm{m/s}$, whereas at $p = 0.4$, perturbations are strongly damped, the terminal speed dispersion falls to $0.109\ \mathrm{m/s}$, and the minimum simulated headway increases to $12.90\ \mathrm{m}$. The main contribution is not a new optimal-velocity law, but a penetration-scaled mean-field closure that combines anticipative headway correction and cooperative speed-difference damping in an analytically tractable form, yielding an explicit critical-penetration formula and stability maps. The reported minimum headway is used only as a spacing-regularity indicator and operational surrogate; it should not be interpreted as a formal safety guarantee.

Keywords: mixed-autonomy traffic; car-following model; nonlinear dynamics; stability threshold; connected and autonomous vehicles; intelligent transportation
Mathematics Subject Classification: 34D20, 37N15, 90B20, 93D20

1. Introduction

Traffic oscillations that emerge without bottlenecks or lane changes remain one of the most characteristic phenomena in transportation dynamics. Such stop-and-go waves arise from microscopic driver interactions, but their collective effect is macroscopic: reduced average speed, excessive braking, elevated fuel use, and more compressed vehicle spacings. Classical nonlinear car-following models, especially the optimal-velocity family introduced by Bando et al. [1] and the full velocity-difference framework of Jiang et al. [2], established that phantom jams can appear purely from endogenous instability of uniform flow. These models remain influential because they are mathematically transparent and sufficiently rich to reproduce realistic wave formation. Early car-following formulations [3,4], kinematic-wave models [5,6], and second-order continuum models [7,8] provide the broader analytical background for understanding endogenous congestion growth and wave propagation.

The arrival of connected and autonomous vehicles (CAVs) has transformed this classical problem into one of mixed-autonomy traffic stability. Although CAVs can preview traffic states and provide cooperative damping, practical traffic streams will contain human-driven and autonomous vehicles for an extended transition period. Talebpour and Mahmassani [9] showed that increasing CAV penetration can improve stability and throughput in mixed traffic, while Stern et al. [10] demonstrated experimentally that even a small amount of automated control can dissipate stop-and-go waves on a ring road. Together, these studies suggest that the onset and suppression of traffic waves depend on how autonomous penetration and control strength are incorporated into the traffic dynamics. Related studies show that ACC/CACC systems and traffic-jam control can influence traffic-flow stability and oscillation damping [11–13], while delayed-feedback, mixed-autonomy, and string-stability analyses provide complementary support [14–16]. Ring-road stability and reaction-time/anticipation studies further motivate the preview-based mechanism adopted here [17,18], whereas empirical commercial ACC may exhibit weak string stability or reduced capacity [19].

Studies directly related to this problem have examined penetration rate and anticipation/communication effects in heterogeneous mixed traffic. Zhai et al. [20] proposed a multi-phase heterogeneous traffic-flow model for HDV/CV environments and showed that connected-vehicle penetration and the perceived range of preceding vehicles are important for bottleneck suppression and stability. Jiao et al. [21] investigated nonlinear taillight effects in mixed traffic driven by competing visual delay and V2X communication, highlighting the role of anticipation and communication in traffic-wave dynamics.

Broader transportation applications of mathematical modeling, including traffic-system dynamics and transportation optimization [22,23], accident prediction, vehicle perception, adverse-weather sensing [24–26], and dynamic traffic assignment [27], are retained only as methodological background. To make the review more targeted, the following discussion is centered on mixed-flow car-following stability, penetration-dependent thresholds, and anticipative or communication-based control.

In this work, we address this focused line of mixed-traffic car-following stability research by developing a parsimonious nonlinear mean-field penetration model that remains analytically tractable. Rather than constructing a highly detailed engineering simulator, we focus on a compact mathematical structure capable of explaining how partial CAV penetration modifies the onset and suppression of traffic waves. The central idea is to represent mixed autonomy through two penetration-dependent mechanisms: An anticipative correction in the effective headway and a cooperative damping term in the relative speed. This modeling choice enables the autonomous content of the traffic stream to enter the nonlinear dynamics and the linear stability theory explicitly. As a result, the framework supports closed-form equilibrium analysis, an explicit characteristic equation, a long-wave stability condition, and a closed-form critical-penetration formula. Furthermore, it remains compatible with related mathematical treatments of continuum-car-following equivalence [28], delay-aware traffic models [29], and ring-road/string-stability analysis [17,30].

To clarify the novelty, the formulation inherits the optimal-velocity relaxation structure and the velocity-difference feedback idea, whereas the new component is the p-scaled mean-field closure that causes penetration to enter the characteristic equation and the closed-form threshold explicitly.

The remainder of this paper is organized as follows: In Section 2, we present the model formulation. In Section 3, we derive the homogeneous equilibrium and present the linear stability analysis. In Section 4, we examine the critical penetration threshold and stability maps. In Section 5, we describe the numerical experiment design. In Section 6, we report simulation results and robustness analyses. In Sections 7 and 8, we provide the discussion and conclusions.

2. Model formulation

Consider N vehicles moving on a single-lane ring road of length L. Vehicle overtaking is excluded, and the vehicle order is preserved. Let $x_n(t)$ denote the longitudinal position of vehicle n, let $s_n(t) = x_{n+1}(t) - x_n(t)$ be the headway, and let $v_n(t) = \dot{x}_n(t)$ be the speed. Periodicity is imposed by identifying x_{N+1} with $x_1 + L$. The baseline equilibrium spacing is $h = \frac{L}{N}$, and the corresponding equilibrium density is $\rho = \frac{N}{L} = \frac{1}{h}$. To focus on the mathematical influence of autonomy rather than on a detailed communication topology, we introduce a mean-field closure in which the penetration ratio $p \in [0,1]$ scales the autonomous contribution to the control law.

Two mechanisms are introduced. The first is an anticipative headway correction: A larger p increases the extent to which the driver-controller responds not only to the current headway s_n but also to the local headway gradient $s_{n+1} - s_n$. The second is a cooperative damping term proportional to the relative speed $v_{n+1} - v_n$. When $p = 0$, the model reduces to a classical optimal-velocity mechanism. As p increases, the traffic stream receives progressively stronger preview and damping, which together represent an averaged preview-and-damping effect of connected/autonomous information rather than a specific heterogeneous arrangement or communication topology.

The optimal-velocity relaxation term is inherited from classical OVM-type models, and the speed-difference feedback is related to FVD and ACC/CACC-type mechanisms. The novelty of Eq (2) is the joint p-scaled mean-field formulation of these two channels, rather than either component alone.

The mean-field closure should be read as a penetration-level approximation rather than an explicit assignment of vehicle types. For a fixed value of p, an actual heterogeneous traffic stream may contain evenly spaced CAVs, random CAV locations, or clustered CAV platoons; such arrangements can create different local interaction chains and communication paths. This model averages these configuration-specific effects into effective penetration-scaled preview and damping gains. Hence, it is intended to capture the aggregate stability tendency and to support a closed-form threshold, not to replace a placement-specific heterogeneous simulation [9,15,16].

Therefore, p should be interpreted as an aggregate autonomy intensity rather than a microscopic vehicle label. The model is most suitable for traffic streams in which CAV effects are sufficiently dispersed or averaged over space. It is less suitable for evaluating stability differences among specific

CAV placement patterns, such as uniformly spaced CAVs, randomly scattered CAVs, or clustered CAV platoons.

The anticipative headway correction has the form $s_{\mathrm{n}} + \sigma p(s_{\mathrm{n+1}} - s_{\mathrm{n}})$ because $s_{\mathrm{n+1}} - s_{\mathrm{n}}$ is the simplest local spatial-gradient indicator available in a nearest-neighbor ring model. If the downstream headway is larger than the current headway, this correction increases the effective spacing perceived by the controller; if the downstream headway is smaller, it reduces the effective spacing and anticipates compression ahead. Factor σ controls how strongly this preview information is used, while multiplication by p ensures that the correction vanishes in the human-driven limit and grows with the aggregate availability of CAV sensing or communication. This form keeps the classical optimal-velocity response as the limiting case p = 0 or σ = 0, while adding the minimal anticipative channel needed for this stability analysis [18].

The cooperative speed-difference damping term $\kappa p(v_{\mathrm{n+1}} - v_{\mathrm{n}})$ is included to represent penetration-scaled relative-speed feedback, a mechanism that is common in velocity-difference and cooperative adaptive cruise-control formulations [2,13]. If the preceding vehicle is faster than vehicle n, the term is positive and helps the follower accelerate smoothly; if the preceding vehicle is slower, the term becomes negative and suppresses the closing speed. Thus, κ controls dissipative coupling, whereas σ controls spatial anticipation. These two mechanisms are written separately because they influence stability through different physical channels: Preview changes the effective headway response, whereas speed-difference feedback directly damps velocity mismatches.

Figure 1 summarizes the modeling philosophy. Table 1 summarizes the notation, meanings, and units used in the model. The human optimal-velocity response remains the backbone of the dynamics, but it is augmented by two terms whose intensity is proportional to p. The first term is anticipative: It uses information on the next headway to regularize the desired-speed response. The second term is dissipative: It damps speed differences between consecutive vehicles. This decomposition is helpful because the first term modifies the effective wave propagation speed, whereas the second term contributes directly to damping.

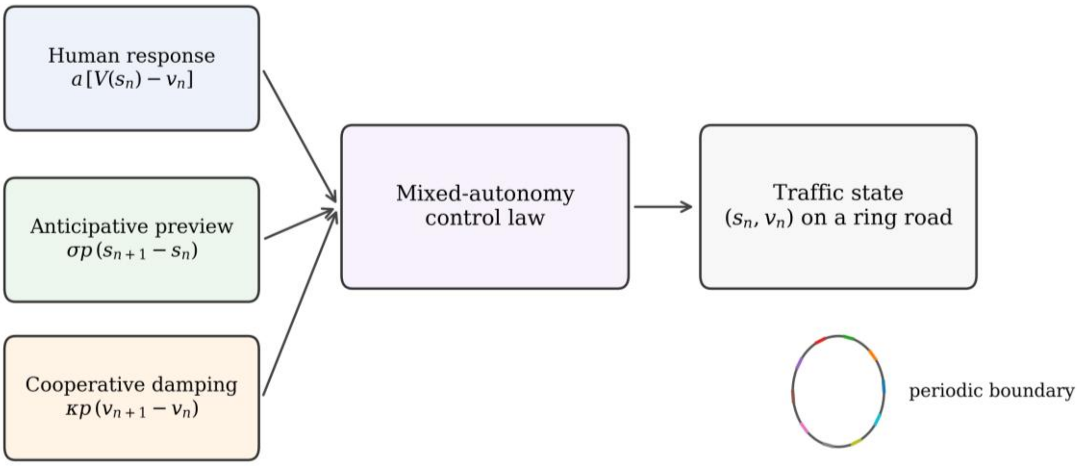

Figure 1. Schematic of the proposed mixed-autonomy traffic model. The human optimal-velocity response is augmented by an anticipative headway correction and a cooperative speed-difference damping term.

Table 1. Main notation used in the proposed model.

Symbol	**Meaning**	**Unit / admissible range**
N	number of vehicles on the ring road	veh
L	ring-road length	m
s_n	headway of vehicle n	m
v_n	speed of vehicle n	m/s
p	CAV penetration ratio	$dimensionless$, [0, 1]
a	human response sensitivity	s^{-1}
σ	anticipative preview weight	$dimensionless, \geq\ 0$
κ	cooperative damping gain	$s^{-1}, \geq 0$
$V(s)$	optimal-velocity function	m/s
V_h	local slope V'(h) at equilibrium	s^{-1}
v_{max}	maximum desired speed in the optimal-velocity function	m/s
s_c	critical spacing parameter in the optimal-velocity function	m
ℓ	smoothing length scale in the optimal-velocity function	$m, >\ 0$

The governing equations are

$$\dot{s}_n = v_{n+1} - v_n, n = 1, \dots, N, \tag{1}$$

$$\dot{v}_n = a[V(s_n + \sigma p(s_{n+1} - s_n)) - v_n] + \kappa p(v_{n+1} - v_n), \tag{2}$$

$$V(s) = \frac{v_{\max}}{2}\left[\tanh\ \left(\frac{s - s_c}{\ell}\right) + \tanh\ \left(\frac{s_c}{\ell}\right)\right]\quad . \tag{3}$$

The governing equations are formulated by extending the classical optimal-velocity and velocity-difference car-following frameworks [1,2]. Equation (1) is the kinematic identity for headway evolution, and Eq (3) adopts a standard smooth optimal-velocity function. The main new component is Eq (2), where the optimal-velocity relaxation and speed-difference feedback are augmented by a penetration-scaled mean-field closure. Specifically, the anticipative headway correction $s_n + \sigma p(s_{n+1} - s_n)$ and the cooperative damping term $\kappa p(v_{n+1} - v_n)$ enable the CAV penetration ratio p to enter the nonlinear dynamics and the subsequent stability threshold explicitly.

Figure 2 displays the chosen optimal-velocity function. The equilibrium headway $h\ =\ 13\ m$ lies in the region where the slope $V'(h)$ is relatively large. This is the mathematically interesting regime: The human-only stream is unstable, but moderate autonomy has a chance to stabilize it. If h were much larger, $V'(h)$ would be too small to trigger amplification; if h were much smaller, the nonlinear slope would be so steep that the chosen damping gains could be insufficient.

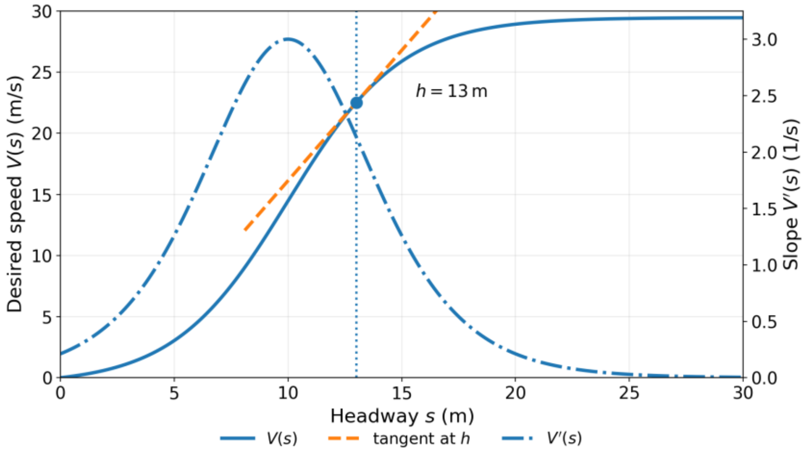

Figure 2. Optimal-velocity function and local slope at the equilibrium spacing $h = 13\ m$. The baseline state is selected in a relatively steep portion of the curve. The baseline parameters used to generate this curve are reported in Table 2.

Table 2. Baseline simulation parameters for the Python experiments.

Parameter	Value (with unit)	Comment
N	$60\ veh$	vehicles on the ring road
L	$780\ m$	total road length
$h = L/N$	$13\ m$	equilibrium spacing
$V(h)$	$22.516\ m/s$	equilibrium speed
a	2.8 s^{-1}	response sensitivity
σ	$0.8\ (dimensionless)$	anticipative weight
κ	2.0 s^{-1}	cooperative damping gain
A	$2.0\ m$	amplitude of sinusoidal headway perturbation
Δt	$0.05\ s$	time step for RK4
T	$300\ s$	total simulation horizon
v_{max}	$30\ m/s$	maximum desired speed in V(s)
s_c	$10\ m$	critical spacing parameter in V(s)
ℓ	$5\ m$	smoothing length scale in V(s)

3. Equilibrium and linear stability analysis

3.1. Homogeneous equilibrium

The homogeneous solution corresponds to $s_n(t) \equiv h$ and $v_n(t) \equiv v^*$ for all vehicles. Because the headway gradient and the relative-speed term vanish in uniform flow, the equilibrium speed is determined solely by the optimal-velocity relation, namely $v^* = V(h)$. This simple structure is useful: The equilibrium remains interpretable, while the penetration ratio modifies the stability of that equilibrium rather than its existence.

In this paper, we use the smooth optimal-velocity function shown in Figure 2. This choice keeps the nonlinear dynamics differentiable, admits an explicit derivative $V_h = V'(h)$, and reproduces the usual fact that sensitivity is largest at intermediate spacing and small at very low and very high densities.

Consequently, the instability window is concentrated around medium-to-high densities, a pattern consistent with traffic intuition and the general nonlinear traffic-flow literature [30–32].

Proposition 3.1. For every spacing $h = L/N > 0$, the mixed-autonomy model admits the homogeneous equilibrium$s_n(t) \equiv h$ and $v_n(t) \equiv V(h)$ for all n = 1, …, N.

Proof. Substituting $s_n \equiv h$ into Eq (1) gives $\dot{s_n} = 0$ because all speeds are equal. Substituting $s_n \equiv h$ and $v_n \equiv V(h)$ into Eq (2) causes the headway-gradient term and the relative-speed term to vanish, and the remaining optimal-velocity relaxation becomes $a[V(h) - V(h)] = 0$. Hence, the uniform branch exists for every admissible h.

To study local stability, we perturb the uniform motion through $x_n(t) = nh + v^* t + y_n(t)$, where y_n is a small displacement variable. Retaining only first-order terms yields the linearized equation displayed below. The coefficient $V_h = V'(h)$ measures the local slope of the optimal-velocity function at the equilibrium spacing. Large V_h means that small headway changes produce large desired-speed corrections, which is precisely the mechanism that creates amplification and traffic waves.

For completeness, the linearization from the displacement perturbation to Eq (4) is written out here. From $x_n(t) = nh + v^* t + y_n(t)$, the perturbed headway and speed are $s_n(t) = h + y_{n+1}(t) - y_n(t)$ and $v_n(t) = v^* + \dot{y}_n(t)$. Therefore, the anticipative spacing argument can be expressed as $h + \delta_n$, where $\delta_n = (y_{n+1} - y_n) + \sigma p (y_{n+2} - 2y_{n+1} + y_n)$. Using the first-order Taylor expansion $V(h + \delta_n) = V(h) + V_h \delta_n + O(\delta_n^2)$, with $V_h = V'(h)$, and using $v^* = V(h)$, all zero-order terms cancel. Keeping only first-order terms gives Eq (4). This step shows explicitly that the anticipative contribution enters through the second spatial difference $y_{n+2} - 2y_{n+1} + y_n$, whereas cooperative damping enters through $\dot{y}_{n+1} - \dot{y}_n$.

The standard Fourier ansatz $y_n(t) = \hat{y} e^{\lambda t + in\theta}$ transforms the linearized chain into a quadratic characteristic equation in the growth rate λ. For a finite ring road, the admissible wave numbers are $\theta_m = \frac{2\pi m}{N}$, $m = 0, 1, \dots, N-1$. The sign of Re (λ) determines whether a mode decays or grows. Instead of relying exclusively on numerical root searches, we further obtain an explicit long-wave approximation by expanding for small θ. This leads to a transport coefficient c_1 and a diffusion-like coefficient c_2. The sign of c_2 is decisive: Negative c_2 implies damping of long-wavelength perturbations, while positive c_2 implies amplification. This spectral viewpoint is standard in mathematical studies of string stability, connected-vehicle delay, and ring-road dynamics [12,14,17].

3.2. Perturbation equation and characteristic polynomial

The local dynamics around the homogeneous equilibrium can be expressed in terms of the displacement perturbation $y_n(t)$. The linearized equation below separates the optimal-velocity response, the anticipative second-difference correction, and the cooperative damping term; it is then converted into a modal characteristic equation by Fourier substitution.

$$\ddot{y}_n = aV_h[(y_{n+1} - y_n) + \sigma p\,(y_{n+2} - 2y_{n+1} + y_n)] - a\dot{y}_n + \kappa p\,(\dot{y}_{n+1} - \dot{y}_n) \tag{4}$$

$$\lambda^2 + [a + \kappa p(1 - e^{i\theta})]\lambda - aV_h[(e^{i\theta} - 1) + \sigma p\,(e^{i\theta} - 1)^2] = 0. \tag{5}$$

Equation (5) is the key algebraic object in the stability analysis. It describes how each Fourier mode responds to the combined effects of nonlinear sensitivity, autonomous preview, and cooperative damping. Exact spectral stability on a finite ring road is determined by checking the sign of the largest real part over all admissible wave numbers $\theta_m = 2\pi m/N$.

The passage from Eq (4) to Eq (5) follows by applying the Fourier mode $y_n(t) = \hat{y}\ \exp(\lambda t + in\theta)$. Under this substitution, $y_{n+1} - y_n = \left(e^{i\theta} - 1\right) y_n, y_{n+2} - 2y_{n+1} + y_n = \left(e^{i\theta} - 1\right)^2 y_n,\ \dot{y}_{n+1} - \dot{y}_n = \lambda\left(e^{i\theta} - 1\right) y_n$, and $\ddot{y}_n = \lambda^2 y_n$. Dividing by the nonzero modal amplitude gives $\lambda^2 = aV_h\left[\left(e^{i\theta} - 1\right) + \sigma p\left(e^{i\theta} - 1\right)^2\right] - a\lambda + \kappa p\lambda\left(e^{i\theta} - 1\right)$. Moving all terms to the left-hand side yields the characteristic polynomial in Eq (5).

For the finite ring road, the admissible modes are $\theta_m = \frac{2\pi m}{N}, m = 0,1,\dots,N-1$. Mode $m = 0$ corresponds to a neutral uniform translation and is excluded from the stability margin. For each nonzero mode, Eq (5) gives two spectral branches λ_m^+ and λ_m^-. Exact finite-ring stability is therefore checked by $\Lambda_N(p) = \max_{1 \le m \le N-1,\, \pm} \mathrm{Re}\ (\lambda_m^{\pm}(p))$.

3.3. Long-wave expansion

To derive the long-wave coefficients, expand $e^{i\theta} = 1 + i\theta - \frac{\theta^2}{2} + O(\theta^3),\ 1 - e^{i\theta} = -i\theta + \frac{\theta^2}{2} + O(\theta^3)$, and $(e^{i\theta} - 1)^2 = -\theta^2 + O(\theta^3)$. Substituting $\lambda = ic_1\theta + c_2\theta^2 + O(\theta^3)$ into Eq (5) gives, at order $O(\theta)$, $ia(c_1 - V_h)\theta = 0$, and, hence, $c_1 = V_h$. The $O(\theta^2)$ balance is $-c_1^2 + ac_2 + \kappa p c_1 + aV_h\left(\frac{1}{2} + \sigma p\right) = 0$. Substituting $c_1 = V_h$ gives $c_2 = \frac{V_h}{2a}[2V_h - a - 2p(a\sigma + \kappa)]$, which is the coefficient reported in Eq (6).

Because $\mathrm{Re}(\lambda) = c_2\theta^2 + O(\theta^3)$, the sign of c_2 determines whether sufficiently long waves are damped or amplified.

$$c_2 = \frac{V_h}{2a}[2V_h - a - 2p(a\sigma + \kappa)]. \tag{6}$$

The long-wave stability condition therefore becomes

$$2V_h < a + 2p(a\sigma + \kappa). \tag{7}$$

Theorem 3.1. Assume $\mathrm{h} > 0, \mathrm{a} > 0, \kappa \ge 0,\ \sigma \ge 0$, and $\mathrm{V_h} = \mathrm{V}'(\mathrm{h}) > 0$. For long-wave perturbations $\theta \to 0$, the homogeneous solution $\mathrm{s_n} \equiv \mathrm{h}, \mathrm{v_n} \equiv \mathrm{V}(\mathrm{h})$ is linearly stable provided that $2\mathrm{V_h} < \mathrm{a} + 2\mathrm{p}(\mathrm{a}\sigma + \kappa)$.

Proof. Substituting the modal ansatz into the characteristic equation and writing $\lambda = ic_1\theta + c_2\theta^2 + O(\theta^3)$, one matches the coefficients of equal order in θ. The first-order term yields $c_1 = V_h$. The second-order coefficient is precisely the expression shown in Eq (6). Therefore, $c_2 < 0$ is equivalent to inequality (7). Since the real part of λ behaves like $c_2\theta^2$ for small θ, negative c_2 implies decay of long waves and, hence, asymptotic stability of the homogeneous branch in the long-wave regime.

The above calculation also clarifies the roles of the two penetration-scaled mechanisms. The anticipative term contributes through σp in the effective headway-gradient response, while the cooperative speed-difference term contributes through κp in the damping of the modal growth rate. Both terms therefore appear additively in the stabilizing combination $p(a\sigma + \kappa)$ in Eq (6).

4. Critical penetration analysis

4.1. Critical penetration formula

Solving the long-wave stability condition in Eq (7) for p gives the critical penetration threshold

$$p_c = \max\left\{0, \frac{(2V_h - a)}{[2(a\sigma + \kappa)]}\right\}. \tag{8}$$

Formula (8) is useful because it provides an explicit penetration threshold for long-wave stability. Starting from the long-wave stability condition, $2V_h < a + 2p(a\sigma + \kappa)$, and assuming $a\sigma + \kappa > 0$, rearrangement gives $p > (2V_h - a)/[2(a\sigma + \kappa)]$.

Since the physically admissible penetration ratio satisfies $0 \leq p \leq 1$, the threshold is truncated from below at zero, as shown in Eq (8). If $a - 2V_h \geq 0$, then $p_c = 0$, and the uniform flow is already stable in the human-driven limit. Otherwise, a positive amount of autonomy is required. If the right-hand side of Eq (8) exceeds one, the selected preview and damping gains are insufficient to stabilize the long-wave mode within the admissible penetration range.

For the baseline parameters used in this paper, namely $N = 60, L = 780\,\mathrm{m}, h = 13\,\mathrm{m}, a = 2.8, \sigma = 0.8, \kappa = 2.0$, Eq (8) gives the asymptotic threshold $p_{c,\mathrm{asy}} = 0.173$, the exact discrete threshold $p_{c,\mathrm{num}}$ is obtained independently from the finite-ring spectrum by solving Eq (5) at every admissible $\theta_m = \frac{2\pi m}{N}$, and then locating the smallest p for which $\Lambda_N(p) < 0$. This computation gives $p_{c,\mathrm{num}} \approx 0.171$.

Remark 4.1. The long-wave threshold $p_{c,\mathrm{asy}}$ and the exact finite-ring threshold $p_{c,\mathrm{num}}$ are related but not identical objects. The former is obtained from the asymptotic limit $\theta \to 0$ and is controlled by the sign of c_2. The latter uses the full quadratic characteristic equation for the discrete set $\theta_m = \frac{2\pi m}{N}$. In the baseline case, the critical finite-ring mode is the lowest nonzero mode, $\theta_1 = \frac{2\pi}{60} \approx 0.105$, so the small-$\theta$ expansion gives a close estimate of the exact spectrum. This is why $p_{c,\mathrm{asy}} \approx 0.173$ and $p_{c,\mathrm{num}} \approx 0.171$ are nearly the same.

The approximation should be interpreted with this modal relationship in mind. The long-wave formula is expected to be most reliable when the dominant unstable mode is a low-wavenumber perturbation, the ring has sufficiently many vehicles, and the traffic state remains close to the homogeneous equilibrium. If the ring is very short, if a higher discrete wave number becomes dominant, or if nonlinear finite-amplitude disturbances move the system far from equilibrium, the exact discrete spectrum and direct simulation should be used in conjunction with the long-wave formula.

4.2. Stability maps

Figure 3 shows the asymptotic stability map in the (p, κ)-plane for the baseline spacing. The neutral curve separates an unstable low-gain region from a stable high-gain region. For $\kappa = 2.0$, the model predicts a threshold close to $p = 0.17$. This plot can also be interpreted as a control-design diagram: If autonomous penetration is low, a larger cooperative gain is required; if the available gain is limited, a larger penetration is required.

Figure 4 extends the analysis to the density-penetration plane at fixed κ. The unstable zone is concentrated around medium and high densities, precisely where the optimal-velocity slope is largest.

At lower densities, the uniform branch is naturally stable even without autonomy, because the desired-speed function becomes flatter. Conversely, very dense regimes near the steepest part of the curve may remain difficult to stabilize, indicating that penetration and gain design must be considered jointly. This interpretation is also consistent with classical continuum and non-equilibrium traffic formulations [5,7,8], as well as related continuum and delay-aware traffic models [15,28,29].

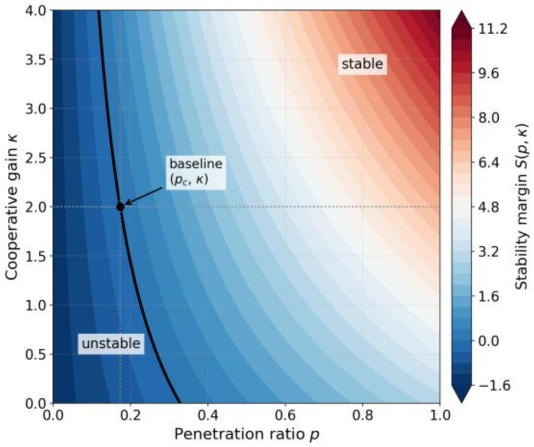

Figure 3. Asymptotic stability margin in the penetration-gain plane at the baseline spacing. The neutral curve predicts the control effort required to stabilize uniform flow. The baseline spacing is h = 13 m, and the neutral curve corresponds to the long-wave stability condition (7).

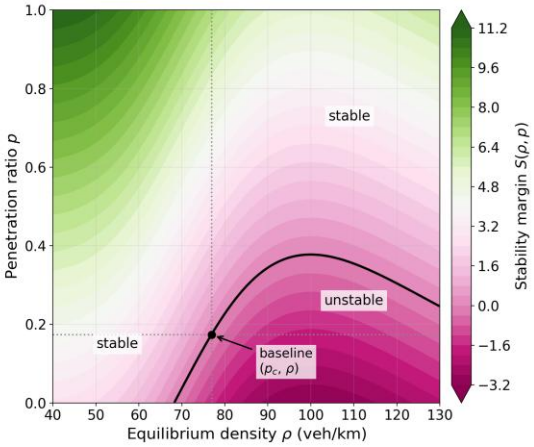

Figure 4. Stability phase map in the density-penetration plane for $\kappa = 2.0$. The unstable region concentrates around densities for which the slope of the optimal-velocity function is large. Unless otherwise stated, the remaining parameters are fixed at the baseline values in Table 2.

These analytical thresholds and stability maps motivate the numerical experimental design described in the next section.

5. Numerical experimental design

5.1. Numerical method and diagnostic indicators

For numerical verification, we integrate the headway-speed form of the model rather than the position-speed form. This avoids accumulation error in the periodic closure and preserves the total road length exactly after a mild numerical renormalization of the headway vector. Time integration is performed with the classical fourth-order Runge-Kutta method. The implementation is concise and reproducible in Python; the accompanying script reproduces all simulation figures and tabulated metrics.

The initial condition is a sinusoidal perturbation around the uniform spacing: $s_n(0) = h + Asin(2\pi n/N)$, with $A = 2\ m$ and $v_n(0) = V(h)$. This mode is deliberately chosen because it excites the long-wave mechanisms analyzed in Section 3. The simulation horizon is $T = 300\ s$ with time step $\Delta t = 0.05\ s$. To compare penetration levels, we evaluate the terminal speed dispersion Σ_v, the minimum headway over the last 60 s, and the mean speed over the same time window. We also compute the exact spectral growth rate $\Lambda(p) = max_m Re(\lambda_m)$ from the discrete characteristic equation for direct comparison with the simulated long-time behavior. The chosen ring-road perturbation setting is consistent with earlier experimental and theoretical benchmarks for stop-and-go-wave generation and attenuation [10,12,17].

The proposed diagnostics play different roles. The mean speed reflects macroscopic efficiency. The speed dispersion measures whether a coherent wave pattern persists. The minimum headway is reported as a spacing-compression indicator and an operational surrogate for headway regularity, because severe stop-and-go oscillations tend to compress headways somewhere in the vehicle string. It is not used as a formal safety metric. Taken together, these indicators reveal whether a penetration level is not only mathematically stable but also associated with smoother and more regular traffic operation.

5.2. Computational workflow

The numerical workflow consists of four steps. Step 1: Initialize the headway vector by a sinusoidal perturbation around h and set the speed vector to the equilibrium value $\mathrm{V}(h)$. Step 2: Advance the state with one fourth-order Runge-Kutta step using Eqs (1) and (2). Step 3: Renormalize the headway vector so that its average remains exactly h. Step 4: Compute diagnostic metrics and, in parallel, evaluate the exact spectral growth rate from Eq (5). This workflow is simple enough to be implemented in a short Python script, yet it provides the figures and tables required for the manuscript.

6. Simulation results and robustness analysis

6.1. Baseline simulation results

Figure 5 gives the clearest visual confirmation of the theory. In the purely human-driven case $p = 0$, a coherent stop-and-go wave emerges and propagates backward around the ring road. The wave band is sharp and persistent, which is typical of nonlinear traffic instabilities. In contrast, when the mean-field penetration level is set to $p = 0.4$, the initial disturbance is rapidly dissipated and the speed field becomes nearly uniform over the whole ring.

It should be emphasized that the penetration ratio used in these simulations is a mean-field penetration level. Thus, the transition from persistent waves to perturbation damping reflects the aggregate preview-and-damping effect of CAV participation, not a comparison among specific microscopic CAV arrangements. For the same p, different heterogeneous placements may produce different local stability behavior, especially when CAVs are clustered or communication topology is restricted.

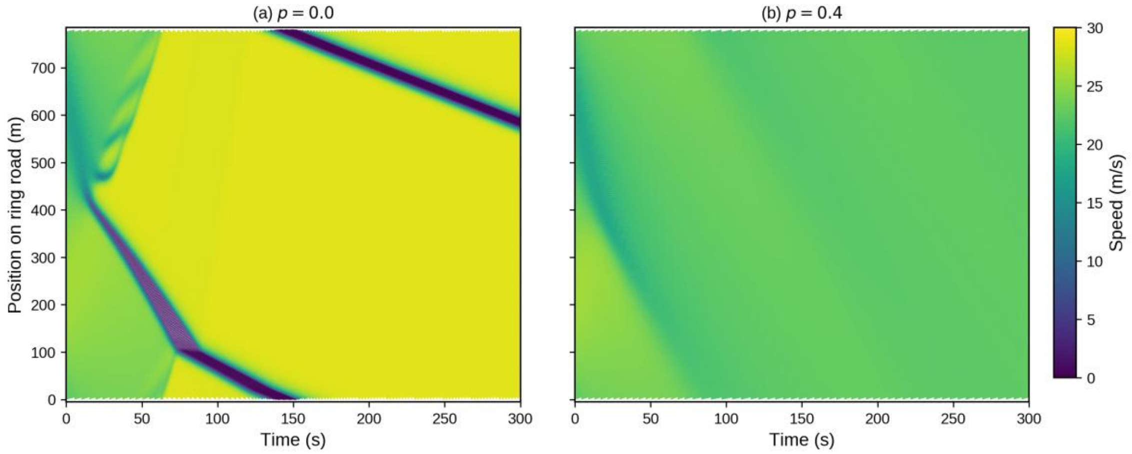

Figure 5. Space-time speed maps for the ring-road simulations. The human-only case develops a self-sustained backward-moving traffic wave, whereas the $p = 0.4$ case exhibits rapid dissipation of the initial perturbation. Both panels use the baseline parameters in Table 2, the sinusoidal initial perturbation with A = 2 m, and the simulation horizon T = 300 s.

Figure 6 reports the temporal evolution of the velocity-dispersion measure for representative penetration ratios. In the human-driven limit $p = 0$, the dispersion increases rapidly and saturates near 13 m/s, confirming the persistence of a pronounced stop-and-go pattern. At $p = 0.2$, which lies only slightly above the exact threshold of approximately 0.171, the perturbation decays only after a comparatively long transient, and the terminal dispersion remains small but not negligible over the finite horizon $T = 300\ s$. This response is therefore more appropriately interpreted as near-neutral and weakly stable, rather than genuinely unstable. For $p \geq 0.4$, the dispersion decreases rapidly to an almost zero level. The comparison shows that a larger mean-field penetration level not only stabilizes the uniform flow but also shortens the relaxation time required to recover the homogeneous state.

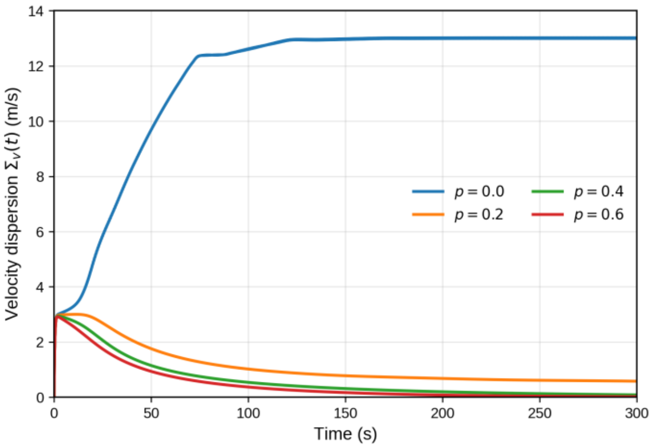

Figure 6. Time evolution of the velocity-dispersion indicator for representative penetration ratios. Increasing penetration accelerates perturbation damping and reduces the terminal oscillation amplitude. All curves use the baseline parameters in Table 2; the dispersion indicator is evaluated over the same 300-s simulation horizon.

The terminal headway profiles in Figure 7 provide a complementary microscopic view of the same transition. When $p = 0$, the final state is strongly heterogeneous, with compressed gaps inside the congested region and enlarged gaps elsewhere; this pattern is characteristic of a self-sustained stop-and-go wave. At $p = 0.2$, the profile becomes markedly smoother but still departs from the uniform equilibrium configuration, again suggesting proximity to the stability boundary. For $p = 0.4$ and $p = 0.6$, the headways cluster tightly around the equilibrium value h, demonstrating that the averaged preview-and-damping feedback suppresses spatial irregularity in the mean-field simulation and restores an almost homogeneous profile. Accordingly, the smoother headway profiles should be interpreted as mean-field responses of the averaged model rather than as predictions for every possible spatial arrangement of CAVs.

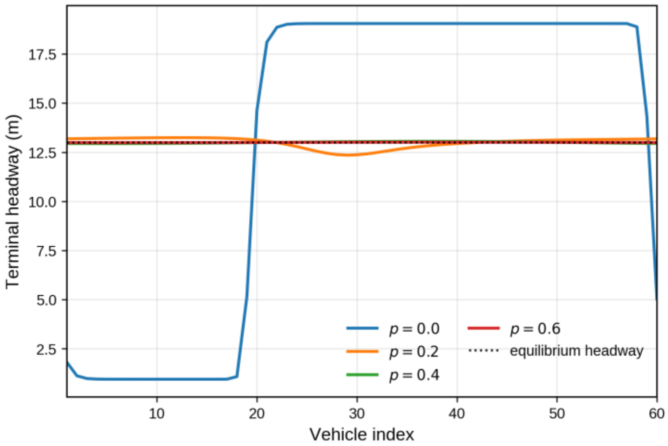

Figure 7. Terminal headway profiles at $t = 300\ s$ for representative penetration ratios. Above the critical penetration level, the heterogeneous jam pattern is replaced by an almost uniform equilibrium spacing. All terminal profiles are evaluated at t = 300 s under the baseline ring-road setting.

The aggregate performance metrics reported in Figure 8 and Table 3 enable the numerical results to be summarized succinctly. The exact spectral growth rate $\Lambda(p)$ changes sign near the analytical threshold, whereas the empirical indicators improve progressively with increasing aggregate penetration. In particular, the mean speed recovers to a value close to $V(h)$ once p reaches 0.2, the terminal speed dispersion decreases by roughly two orders of magnitude between $p = 0$ and $p = 0.4$, and the minimum headway rises from less than 1 m in the unstable regime to approximately 12.9 m in the stable cases. These trends show that the theoretical stability threshold has a clear operational interpretation: A higher aggregate penetration level improves flow regularity and reduces severe spacing compression under the proposed mean-field closure. The increase in minimum headway should therefore be interpreted as an improvement in spacing regularity, not as a rigorous safety guarantee. Thus, the numerical indicators are mean-field stability indicators; explicit heterogeneous simulations would be required to compare uniform, random, and platoon-based CAV distributions.

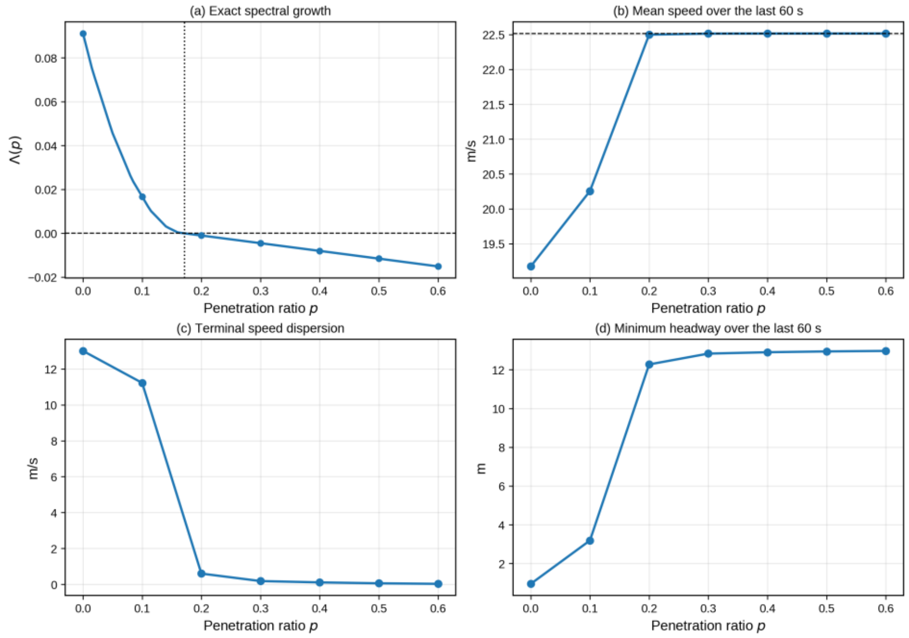

Figure 8. Sensitivity of theoretical and empirical performance metrics to the penetration ratio. The theoretical growth rate changes sign near the analytical threshold, while the simulated indicators improve progressively as p increases. The empirical indicators are computed over the last 60 s of the 300-s simulations.

Table 3. Exact spectral growth and numerical performance over the last 60 s.

p	max Re(λ) (s^{-1})	$\bar{v}$ (m/s)	Σ_v (m/s)	$s_{\min}$ (m)
0.0	0.0911	19.174	13.008	0.950
0.2	-0.0010	22.499	0.600	12.275
0.4	-0.0080	22.516	0.109	12.904
0.6	-0.0151	22.516	0.029	12.972

Note. All numerical performance metrics in Table 3 are evaluated over the last 60 s of the 300-s simulation horizon; unlisted parameters are fixed at the baseline values in Table 2.

6.2. Ablation analysis

To evaluate the relative contribution of the two penetration-scaled mechanisms, an ablation experiment is added at $p = 0.4$. Four cases are compared under the same ring-road setting and perturbation amplitude: The full model, the anticipation-only model with $\kappa = 0$, the damping-only model with $\sigma = 0$, and the classical OVM-type baseline with $\sigma = 0$ and $\kappa = 0$. The same diagnostic indicators and finite-ring spectral calculation are used for all cases.

Table 4 shows that the full model has the lowest critical penetration threshold, with $p_{c,\text{asy}} = 0.173$ and $p_{c,\text{num}} = 0.171$. When the damping term is removed, the threshold increases to $p_{c,\text{asy}} = 0.328$, indicating that anticipative preview alone can stabilize the long-wave mode but requires a higher CAV penetration level. When the anticipative term is removed, the threshold further increases to $p_{c,\text{asy}} = 0.367$, and the last-60-s averaged speed dispersion remains much larger than that of the full model. The classical OVM-type baseline has no penetration-dependent stabilizing mechanism, so no attainable penetration threshold is obtained within this ablation setting. This ablation comparison isolates the two mean-field control channels and does not imply that every physical arrangement of CAVs with the same penetration rate will produce identical decay rates.

Table 4. Ablation comparison for the relative contributions of anticipative preview and cooperative damping at $p = 0.4$.

Ablation case	$\boldsymbol{\sigma}$	$\boldsymbol{\kappa}$ (s^{-1})	$\boldsymbol{p_{c,\mathrm{asy}}}$	$\boldsymbol{p_{c,\mathrm{num}}}$	**max Re(λ) at p=0.4 (s^{-1})**	$\bar{v}$ **(m/s)**	Σ_v **(m/s)**	$s_{\min}$ **(m)**
Full model	0.8	2.0	0.173	0.171	-0.0080	22.516	0.109	12.904
Anticipation only	0.8	0.0	0.328	0.322	-0.0014	22.513	0.231	12.759
Damping only	0.0	2.0	0.367	0.363	-0.0006	21.277	8.497	4.935
Classical OVM	0.0	0.0	N.A.	N.A.	0.0911	19.174	13.008	0.950

Note. The ablation comparison in Table 4 is conducted at p = 0.4 under the baseline ring-road setting; only the displayed preview and damping channels are varied.

The closeness between the theoretical threshold and the numerical threshold under the baseline setting can also be explained by the modal structure of the experiment. The imposed initial perturbation is the fundamental sinusoidal mode of the ring road, and for $N = 60$, the lowest nonzero wave number is $\theta_1 = 2\pi/60 \approx 0.105$, which lies within the small-θ regime used in the long-wave expansion. Therefore, the dominant unstable or weakly stable mode in the finite ring is close to the asymptotic mode used to derive $p_{c,\mathrm{asy}}$. This is why the closed-form threshold $p_{c,\mathrm{asy}} = 0.173$ is very close to the exact finite-ring threshold $p_{c,\mathrm{num}} \approx 0.171$. The agreement should not be interpreted as universal; it is expected to be strongest when the leading mode is a low-wavenumber perturbation, the disturbance amplitude remains moderate, and the dynamics stay close to the homogeneous equilibrium.

The ablation results also make the physical interpretation of the baseline simulation clearer. At $p = 0.4$, the full model has max Re $(\lambda) = -0.008$, which corresponds to a visibly faster damping process than the anticipation-only and damping-only cases, whose growth rates are only weakly negative. Consequently, the full model reaches a last-60-s averaged speed dispersion of $0.109\ \mathrm{m/s}$, whereas the anticipation-only and damping-only cases remain at $0.231\ \mathrm{m/s}$ and $8.497\ \mathrm{m/s}$, respectively. The relatively large value in the damping-only case reflects its near-neutral finite-horizon response under the selected perturbation and simulation horizon. Thus, the numerical superiority of the full model is not merely a graphical trend; it follows from the additive stabilizing contribution of the anticipative and damping terms in the modal growth rate.

6.3. Sensitivity analysis for response sensitivity and anticipative weight

To examine robustness, a one-factor sensitivity analysis is conducted for the response sensitivity a and anticipative preview weight σ. In each test, one parameter is varied while the remaining baseline settings are fixed, and $p = 0.4$ is used for the nonlinear ring-road simulations. Figure 9 compares the asymptotic threshold $p_{c,\mathrm{asy}}$, exact finite-ring threshold $p_{c,\mathrm{num}}$, and exact spectral growth rate $\Lambda_N(0.4)$ under different values of a and σ. Table 5 summarizes the corresponding thresholds, growth rates, mean speeds, last-60-s speed dispersions, and minimum headways.

The results show that $p_{c,\mathrm{asy}}$ and $p_{c,\mathrm{num}}$ remain below $p = 0.4$, while $\Lambda_N(0.4) < 0$ for all tested cases. Increasing a or σ decreases the critical threshold and enhances damping through the stabilizing combination $a\sigma + \kappa$ in Eq (6). The nonlinear simulations confirm the spectral results, indicating that the main stability conclusion is not restricted to the baseline choice $a = 2.8$ and $\sigma = 0.8$, although it should be interpreted within the tested ranges and the present ring-road setting. These robustness results demonstrate parameter robustness within the mean-field closure; they do not replace a placement-specific sensitivity analysis involving explicit CAV/HDV distributions or communication topologies.

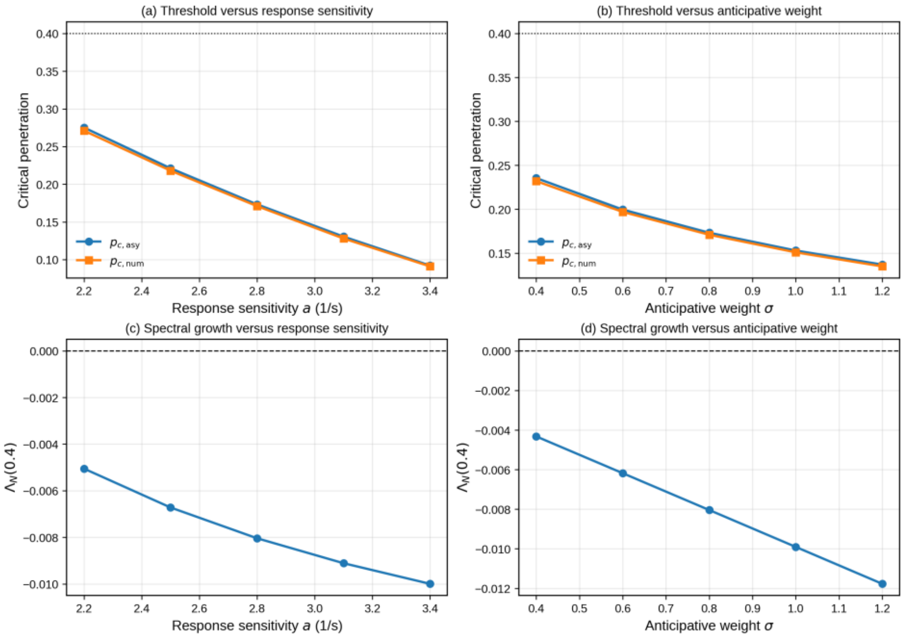

Figure 9. Sensitivity of asymptotic and exact finite-ring critical penetration thresholds and exact spectral growth rate to response sensitivity a and anticipative preview weight σ. Panels (a) and (b) compare $p_{c,\mathrm{asy}}$ and $p_{c,\mathrm{num}}$, respectively, while panels (c) and (d) report $\Lambda_N(0.4)$. The horizontal dotted line in panels (a) and (b) marks the tested penetration $p = 0.4$. Unless varied, all parameters are fixed at the baseline values in Table 2; the nonlinear simulations use p = 0.4.

Table 5. Parameter sensitivity analysis at p = 0.4. Each block varies one parameter while keeping the others at the baseline values in Table 2.

Sensitivity parameter	**Value**	$p_{c,asy}$	$p_{c,num}$	$\Lambda_N(0.4)$ (s^{-1})	$\bar{v}$ **(m/s)**	Σ_v **(m/s)**	$s_{\min}$ **(m)**
Response sensitivity a	2.2	0.275	0.271	-0.0051	22.515	0.170	12.845
	2.8	0.173	0.171	-0.0080	22.516	0.109	12.904
	3.4	0.092	0.091	-0.0100	22.516	0.077	12.930
Anticipative weight σ	0.4	0.235	0.232	-0.0043	22.514	0.187	12.829
	0.8	0.173	0.171	-0.0080	22.516	0.109	12.904
	1.2	0.137	0.135	-0.0118	22.516	0.055	12.948

Note. Table 5 reports one-factor tests at p = 0.4. Unless the listed parameter is varied, all unlisted parameters are fixed at Table 2; nonlinear metrics are evaluated over the last 60 s of the 300-s horizon.

6.4. Additional robustness and baseline-model comparison

To further test whether the numerical conclusions depend on a single baseline configuration, additional one-factor robustness tests are conducted for the cooperative damping gain κ, equilibrium spacing h, perturbation amplitude A, and number of vehicles N. Except for the parameter being varied, all settings are kept at their baseline values, and the tested penetration level is fixed at p = 0.4.

Table 6 shows the sensitivity results for κ and h. The exact spectral growth rate remains negative for all tested cases. Increasing κ lowers the critical threshold and reduces speed dispersion. Changing h modifies the optimal-velocity slope and therefore the critical threshold; the smaller-spacing case h = 11 m remains stable at p = 0.4 but has a larger finite-horizon dispersion.

Table 6. Additional sensitivity analysis for κ and h at p = 0.4. The table separates cooperative-gain and spacing effects while keeping other settings fixed.

Parameter	Value	$p_{c,\text{asy}}$	$p_{c,\text{num}}$	$\Lambda_N(0.4)$ (s^{-1})	Σ_v (m/s)	$s_{\min}$ (m)
	1.0	0.227	0.223	-0.0047	0.178	12.838
κ	2.0	0.173	0.171	-0.0080	0.109	12.904
	3.0	0.140	0.138	-0.0114	0.060	12.945
	11.0	0.350	0.344	-0.0026	1.036	10.204
$h\ (m)$	13.0	0.173	0.171	-0.0080	0.109	12.904
	17.0	0.000	0.000	-0.0062	0.080	16.786

Note. Table 6 reports one-factor tests at p = 0.4. Unless κ or h is varied, all unlisted parameters are fixed at Table 2; Σv and smin are evaluated over the last 60 s.

Table 7 summarizes the robustness tests for A and N. Varying A does not change the linear thresholds but affects the nonlinear finite-horizon indicators. Even for A = 4 m, the perturbation is damped under the baseline gains. For N = 120, the spectral growth rate is closer to zero, so the same 300-s horizon shows slower observable decay than the N = 60 case.

Table 7. Additional sensitivity analysis for A and N at p = 0.4. The table separates perturbation-amplitude and finite-ring-size effects.

Parameter	Value	$p_{c,\text{asy}}$	$p_{c,\text{num}}$	$\Lambda_N(0.4)$ (s^{-1})	Σ_v (m/s)	$s_{\min}$ (m)
	0.5	0.173	0.171	-0.0080	0.070	12.940
A (m)	1.0	0.173	0.171	-0.0080	0.097	12.916
	2.0	0.173	0.171	-0.0080	0.109	12.904
	4.0	0.173	0.171	-0.0080	0.114	12.900
	30	0.173	0.163	-0.0322	0.000	12.999
N	60	0.173	0.171	-0.0080	0.109	12.904
	120	0.173	0.173	-0.0020	0.459	12.599

Note. Table 7 reports one-factor tests at p = 0.4. Linear thresholds are unaffected by A, whereas N changes the finite-ring spectrum; Σv and smin are evaluated over the last 60 s.

A comparison with classical baseline models is also added to distinguish the proposed mechanism from standard OVM and FVD-type dynamics [1,2]. The FVD-type baseline uses a matched velocity-difference damping intensity γ = κp = 0.8 at p = 0.4, but it does not include the anticipative headway correction. Thus, the comparison isolates the added contribution of the penetration-scaled anticipative closure.

Table 8 shows that the classical OVM remains unstable, while the FVD-type baseline is only weakly stable and retains a large speed dispersion over the finite simulation horizon. In contrast, the proposed full model has a more negative spectral growth rate and a much smaller last-60-s speed dispersion. This indicates that the improved stability is not due only to a conventional velocity-difference term, but to the combined penetration-scaled preview and damping structure.

Table 8. Comparison with classical OVM and FVD-type baseline models at p = 0.4. This comparison isolates the contribution of the penetration-scaled anticipative closure.

Model	**Main mechanism**	$\Lambda_N(0.4)$ (s^{-1})	$\bar{v}$ **(m/s)**	Σ_v **(m/s)**	$s_{\min}$ **(m)**
Classical OVM	OVM relaxation only	0.0911	19.174	13.008	0.950
FVD-type baseline	OVM + matched velocity-difference damping	-0.0006	21.277	8.497	4.935
Proposed full model	OVM + p-scaled anticipation and damping	-0.0080	22.516	0.109	12.904

Note. Table 8 uses the same ring-road setting and p = 0.4 for all baseline-model comparisons; empirical metrics are evaluated over the last 60 s.

7. Discussion

This model is intentionally compact. Its main purpose is not to reproduce every aspect of autonomous driving, but to provide a mathematically manageable bridge between nonlinear car-following theory and modern mixed-autonomy questions. This choice brings several advantages. The model admits a closed-form equilibrium, an explicit characteristic equation, a readable long-wave stability theorem, and a direct numerical implementation. Such transparency is often lost in high-fidelity engineering simulators.

The theoretical implication of the closed-form threshold is that CAV penetration does not stabilize traffic as an isolated factor; rather, it works jointly with anticipative preview, cooperative damping, and the local slope of the optimal-velocity function. In particular, the long-wave coefficient shows that the stabilizing effect enters through the combined term $p(a\sigma + \kappa)$. Thus, a lower penetration level may still be effective when preview and damping gains are sufficiently strong, whereas a higher penetration level may be insufficient if the effective gains are weak or if V_{h} is large. From a practical perspective, the threshold and stability maps can be regarded as first-stage screening tools for controller tuning and deployment planning, rather than as deployment guarantees.

Furthermore, the model has limitations that should be acknowledged. The penetration ratio p enters through a mean-field closure rather than through an explicit heterogeneous assignment of human-driven and autonomous vehicles. This is appropriate for deriving aggregate thresholds, but it does not distinguish platoon configurations or communication topologies. Moreover, we study a single-lane ring road without lane changes, merges, or exogenous bottlenecks. Therefore, the results should be interpreted as aggregate mean-field indicators rather than placement-specific predictions.

More specifically, the same penetration rate may correspond to uniformly distributed CAVs, randomly scattered CAVs, or clustered platoons, and these arrangements may generate different local amplification paths, communication chains, and platoon-level stability properties. Explicit heterogeneous simulations are therefore needed to compare CAV placement patterns or communication topologies.

The closed-form critical penetration threshold is expected to be reliable when the dominant unstable mode is a low-wavenumber perturbation, the ring contains sufficiently many vehicles, the disturbance amplitude is moderate, and the dynamics remain close to the homogeneous equilibrium. These conditions are approximately satisfied in the baseline experiment because the imposed perturbation is the fundamental ring-road mode and the exact finite-ring threshold is close to the asymptotic threshold. However, the long-wave approximation may become less reliable for short rings, high-wavenumber disturbances, strongly clustered CAV distributions, large nonlinear perturbations, stochastic reaction or communication delays, actuator saturation, or braking constraints. In such cases, the closed-form threshold should be supplemented by exact finite-spectrum analysis and nonlinear simulation.

These limitations suggest several natural directions for future research. For heterogeneous CAV distributions, scalar penetration ratio p could be replaced by explicit vehicle-type indicators or a spatially varying local penetration field, enabling uniformly distributed, randomly scattered, and clustered CAV patterns to be compared. For stochastic reaction or communication delays, the preview and damping terms could be reformulated as delayed or random feedback terms, and the resulting threshold would need to be examined using delay-aware or stochastic stability analysis. For more realistic road scenarios, this ring-road framework could be extended to open-boundary roads, bottlenecks, merging areas, and multi-lane traffic. These extensions would test whether the proposed closed-form threshold remains a useful local approximation or must be replaced by scenario-specific numerical stability criteria.

8. Conclusions

In this study, we proposed a nonlinear mean-field penetration model for car-following dynamics with anticipative preview and cooperative damping, in which penetration ratio p served as an explicit parameter describing the aggregate CAV content of the traffic stream. Within this framework, the homogeneous equilibrium, perturbation dynamics, characteristic equation, and long-wave stability condition were derived analytically. A major theoretical result was the closed-form critical-penetration formula, which provides a direct stability threshold for the onset or suppression of traffic waves. For the baseline setting, the asymptotic threshold $p_c \approx 0.173$ was close to the exact discrete-spectrum threshold $p_c \approx 0.171$, indicating that the long-wave approximation captures the finite-ring stability boundary with good accuracy. Numerical ring-road simulations further supported the analysis: The human-only stream exhibited persistent stop-and-go waves, whereas mean-field penetration levels above the threshold strongly damped disturbances and restored near-uniform flow under the averaged model. These results showed that a parsimonious mean-field structure can yield explicit thresholds, interpretable stability maps, and a useful control-design perspective while retaining essential nonlinear traffic dynamics. The reported minimum headway should be interpreted only as a spacing-regularity indicator and operational surrogate rather than a formal safety guarantee, since this model does not include vehicle length, explicit collision-avoidance constraints, stochastic reaction delays, or realistic braking limitations. Researchers may extend the framework to explicit heterogeneous CAV placement, stochastic reaction, communication delays, open-boundary and multi-lane road scenarios, collision-aware constraints, and cost-aware optimization of CAV deployment strategies. Such extensions would clarify whether the closed-form threshold remains a useful local design indicator or should be replaced by scenario-specific numerical stability criteria.

Use of Generative-AI tools declaration

The authors declare they have used Artificial Intelligence (AI) tools in the creation of this article.

Acknowledgments

The author would like to thank the National Science and Technology Council, Taiwan, for financially supporting this research (grant No. NSTC 114-2221-E-018-003) and the Ministry of Education's Teaching Practice Research Program, Taiwan (MOE-114-TPRSK-0015-027Y1).

Conflict of interest

The authors declare no conflict of interest.

References

1. M. Bando, K. Hasebe, A. Nakayama, A. Shibata, Y. Sugiyama, Dynamical model of traffic congestion and numerical simulation, *Phys. Rev. E*, **51** (1995), 1035–1042. https://doi.org/10.1103/PhysRevE.51.1035
2. R. Jiang, Q. Wu, Z. Zhu, Full velocity difference model for a car-following theory, *Phys. Rev. E*, **64** (2001), 017101. https://doi.org/10.1103/PhysRevE.64.017101
3. R. Chandler, R. Herman, E. Montroll, Traffic dynamics: studies in car following, *Oper. Res.*, **6** (1958), 165–184. https://doi.org/10.1287/opre.6.2.165
4. G. Newell, Nonlinear effects in the dynamics of car following, *Oper. Res.*, **9** (1961), 209–229. https://doi.org/10.1287/opre.9.2.209
5. M. Lighthill, G. Whitham, On kinematic waves II: a theory of traffic flow on long crowded roads, *Proc. A*, **229** (1955), 317–345. https://doi.org/10.1098/rspa.1955.0089
6. P. Richards, Shock waves on the highway, *Oper. Res.*, **4** (1956), 42–51. https://doi.org/10.1287/opre.4.1.42
7. A. Aw, M. Rascle, Resurrection of "second order" models of traffic flow, *SIAM J. Appl. Math.*, **60** (2000), 916–938. https://doi.org/10.1137/S0036139997332099
8. H. Zhang, A non-equilibrium traffic model devoid of gas-like behavior, *Transport. Res. B- Meth.*, **36** (2002), 275–290. https://doi.org/10.1016/S0191-2615(00)00050-3
9. A. Talebpour, H. Mahmassani, Influence of connected and autonomous vehicles on traffic flow stability and throughput, *Transport. Res. C-Emer.*, **71** (2016), 143–163. https://doi.org/10.1016/j.trc.2016.07.007
10. R. E. Stern, S. Cui, M. L. Delle Monache, R. Bhadani, M. Bunting, M. Churchill, et al., Dissipation of stop-and-go waves via control of autonomous vehicles: field experiments, *Transport. Res. C-Emer.*, **89** (2018), 205–221. https://doi.org/10.1016/j.trc.2018.02.005
11. L. Davis, Effect of adaptive cruise control systems on traffic flow, *Phys. Rev. E*, **69** (2004), 066110. https://doi.org/10.1103/PhysRevE.69.066110
12. G. Orosz, R. Wilson, G. Stépán, Traffic jams: dynamics and control, *Philos. Trans. A Math. Phys. Eng. Sci.*, **368** (2010), 4455–4479. https://doi.org/10.1098/rsta.2010.0205
13. V. Milanés, S. Shladover, Modeling cooperative and autonomous adaptive cruise control dynamic responses using experimental data, *Transport. Res. C-Emer.*, **48** (2014), 285–300. https://doi.org/10.1016/j.trc.2014.09.001
14. J. I. Ge, G. Orosz, Dynamics of connected vehicle systems with delayed acceleration feedback, *Transport. Res. C-Emer.*, **46** (2014), 46–64. https://doi.org/10.1016/j.trc.2014.04.014

15. K. Huang, X. Di, Q. Du, X. Chen, Scalable traffic stability analysis in mixed-autonomy using continuum models, *Transport. Res. C-Emer.*, **111** (2020), 616–630. https://doi.org/10.1016/j.trc.2020.01.007
16. L. Ma, S. Qu, J. Ren, X. Zhang, Mixed traffic flow of human-driven vehicles and connected autonomous vehicles: string stability and fundamental diagram, *Math. Biosci. Eng.*, **20** (2023), 2280–2295. https://doi.org/10.3934/mbe.2023107
17. F. Chou, A. Keimer, A. Bayen, Stability of ring roads and string stability of car following models, *Math. Control Relat. F.*, **14** (2024), 1752–1775. https://doi.org/10.3934/mcrf.2024062
18. M. Treiber, A. Kesting, D. Helbing, Influence of reaction times and anticipation on stability of vehicular traffic flow, *Transport. Res. Rec.*, **1999** (2007), 23–29. https://doi.org/10.3141/1999-03
19. B. Ciuffo, K. Mattas, M. Makridis, G. Albano, A. Anesiadou, Y. He, Requiem on the positive effects of commercial adaptive cruise control on motorway traffic and recommendations for future automated driving systems, *Transport. Res. C-Emer.*, **130** (2021), 103305. https://doi.org/10.1016/j.trc.2021.103305
20. C. Zhai, K. Li, R. Zhang, T. Peng, C. Zong, Phase diagram in multi-phase heterogeneous traffic flow model integrating the perceptual range difference under human-driven and connected vehicles environment, *Chaos Soliton. Fract.*, **182** (2024), 114791. https://doi.org/10.1016/j.chaos.2024.114791
21. S. Jiao, L. Xue, Y. Li, J. Wu, A. Li, Nonlinear dynamics of taillight effect in mixed traffic flow driven by competing visual delay and V2X communication, *Chaos Soliton. Fract.*, **208** (2026), 118152. https://doi.org/10.1016/j.chaos.2026.118152
22. J. Sanchez, A. Valverde, J. Guirao, H. Chen, Mathematical modeling for the development of traffic based on the theory of system dynamics, *AIMS Mathematics*, **8** (2023), 27626–27642. https://doi.org/10.3934/math.20231413
23. J. Chen, Y. Wu, S. Huang, P. Wang, Multi-objective optimization for AGV energy efficient scheduling problem with customer satisfaction, *AIMS Mathematics*, **8** (2023), 20097–20124. https://doi.org/10.3934/math.20231024
24. M. Al-Thani, Z. Sheng, Y. Cao, Y. Yang, Traffic Transformer: transformer-based framework for temporal traffic accident prediction, *AIMS Mathematics*, **9** (2024), 12610–12629. https://doi.org/10.3934/math.2024617
25. T. Vaiyapuri, M. Sivakumar, S. Shridevi, V. Parvathy, J. Ramesh, K. Syed, et al., An intelligent water drop algorithm with deep learning driven vehicle detection and classification, *AIMS Mathematics*, **9** (2024), 11352–11371. https://doi.org/10.3934/math.2024557
26. K. Tarmissi, H. Mengash, N. Negm, Y. Said, A. Al-Sharafi, Explainable artificial intelligence with fusion-based transfer learning on adverse weather conditions detection using complex data for autonomous vehicles, *AIMS Mathematics*, **9** (2024), 35678–35701. https://doi.org/10.3934/math.20241693
27. D. Yan, J. Cheng, J. Gan, Y. Wang, A dynamic traffic assignment model for solving overlapping path issues and perfectly rational issues under stochastic time-varying conditions, *AIMS Mathematics*, **10** (2025), 30661–30682. https://doi.org/10.3934/math.20251345
28. W. Jin, On the equivalence between continuum and car-following models of traffic flow, *Transport. Res. B-Meth.*, **93** (2016), 543–559. https://doi.org/10.1016/j.trb.2016.08.007
29. S. Göttlich, E. Iacomini, T. Jung, Properties of the LWR model with time delay, *Netw. Heterog. Media*, **16** (2021), 31–47. https://doi.org/10.3934/nhm.2020032

30. R. Wilson, J. Ward, Car-following models: fifty years of linear stability analysis—a mathematical perspective, *Transport. Plan. Techn.*, **34** (2011), 3–18. https://doi.org/10.1080/03081060.2011.530826
31. M. Treiber, A. Kesting, *Traffic flow dynamics: data, models and simulation*, Cham: Springer, 2025. https://doi.org/10.1007/978-3-031-93922-8
32. D. Helbing, Traffic and related self-driven many-particle systems, *Rev. Mod. Phys.*, **73** (2001), 1067–1141. https://doi.org/10.1103/RevModPhys.73.1067